climate

MDPI

Article

From Past to Present: Decoding Precipitation Patterns in a Complex Mediterranean River Basin

Nazzareno Diodato [1] and Gianni Bellocchi [1,2,*]

[1] Met European Research Observatory—International Affiliates Program, University Corporation for Atmospheric Research, 82100 Benevento, Italy; scodalabdiodato@gmail.com
[2] Unité Mixte de Recherche sur l'Écosystème Prairial (UREP), INRAE, VetAgro Sup, Université Clermont Auvergne, 63000 Clermont-Ferrand, France
* Correspondence: gianni.bellocchi@inrae.fr

Abstract: Enhancing spatial data attributes is crucial for effective basin-scale environmental modelling and improving our understanding and management of precipitation patterns. In this study, we focused on reconstructing homogeneous areal precipitation data in the complex terrain of the Calore River Basin (CRB) in Southern Italy. Until 1869, weather observations in the region were inconsistent, unstandardised, and lacked coordination, but the establishment of meteorological observatories brought a more unified approach to weather monitoring. We relied on the rainfall data obtained from two of these historical observatories: Benevento (1869–present) and Montevergine (1884–present). We utilised a statistical regression framework that considered rainfall measurements and temporal properties from specific locations to reconstruct and visually analyse the evolution patterns of annual mean areal precipitation (MAP) in the CRB from 1869 to 2020. The analysis revealed that mean MAP decreased from 1153 mm yr^{-1} (1869–1951) to 998 mm yr^{-1} (1952–2020). This decrease was accompanied by a reduction in interannual variability (from 168 mm yr^{-1} to 147 mm yr^{-1} standard deviation), and the difference between the means was significant ($p < 0.0001$), suggesting a sudden shift in the time-series. These findings provide a basis for CRB water resource management and insights for modelling other complex Mediterranean basins.

Keywords: evolution patterns interannual variability; mean areal precipitation; statistical regression framework

check for updates

Citation: Diodato, N.; Bellocchi, G. From Past to Present: Decoding Precipitation Patterns in a Complex Mediterranean River Basin. *Climate* **2023**, *11*, 141. https://doi.org/10.3390/cli11070141

Academic Editor: Nir Y. Krakauer

Received: 31 May 2023
Revised: 30 June 2023
Accepted: 3 July 2023
Published: 4 July 2023

Copyright: © 2023 by the authors. Licensee MDPI, Basel, Switzerland. This article is an open access article distributed under the terms and conditions of the Creative Commons Attribution (CC BY) license (https://creativecommons.org/licenses/by/4.0/).

1. Introduction

Precipitation, occurring at various spatial scales, has a significant influence on ecological processes [1,2], driving the exchange of water storage and energy release during climate fluctuations [3]. However, converting point precipitation measurements from ground gauges to areal precipitation poses a challenge in climatic studies [4–6] and broader ecological implications [1,7,8], including water cycle and hydrological modelling [9–12]. Thus, addressing climate and hydrological issues at the areal scale often requires homogeneous spatially and temporally consistent datasets [13–15]. However, while ecological research routinely relies on in situ precipitation observations, hydrological models operating at the basin scale often face challenges due to the lack of homogeneous pluviometric data [16]. The lack of homogeneity in extended time-series of climate data may arise from the combined effects of station relocations and changes in local features [17]. In fact, over extended periods (e.g., 50–100 years), observing stations may have been moved, sometimes to positions with slight elevation differences. Furthermore, the surrounding vegetation and land-use might have experienced modifications.

In response to the increasing development of models that consider spatio-temporal variations in climate, there is a growing need for techniques that can accurately assess changes in homogeneous areal precipitation [18,19]. The study of mean areal precipitation (MAP) changes focuses on the establishing relationships applicable at the grid-cell or basin

scales of models, enabling their implementation in environmental change processes [20]. A major challenge in predicting MAP changes at scales meaningful for hydrological modelling lies in effectively representing the effects exerted by orographic surfaces and other weather features on an annual time-scale [21].

In recent decades, satellite and remote sensing technology has allowed for high-spatial resolution estimates of precipitation over specific areas, specifically for hydrological and climate studies [22]. However, these data are generally available only after 1990. While global data derived from Global Hydrological Models (GHMs; [23]) have become more accessible, they are not ideal for basin-scale applications due to the coarser resolution [24]. To address the challenge of coarser spatial resolution, Karger et al. [25] used a Model Output Statistics algorithm to correct data from ERA-Interim reanalysis using gauge-derived products from the GPCC and GHCN datasets. However, this approach requires greater computational resources and expertise. Alternatively, stochastic weather generators can generate very long time-series of weather patterns, but they have limited capability in reproducing the interannual variability of MAP [26] (Breinl et al., 2017). For small basins, groups of ground stations remain crucial for understanding the climatic variability of MAP. However, their configurations can change over time, and reliable consistency is not always available for historical periods. Evaluating the spatial variability and trends of MAP in these basins can be approached in two ways [6]. The first involves independently interpolating current rainfall grid surfaces, creating gridded precipitation data to fill gaps in climatic data. This method also facilitates assessing the consequences of precipitation change in unsurveyed regions by generating successive precipitation surfaces [27]. However, this strategy can be time-consuming and may not always be appropriate, especially when there are too few stations to perform interpolation. The second method involves directly interpolating station indices and precipitation, followed by calculating indicators for each grid. However, this technique may struggle to accurately represent the distribution of these indices.

In cases where the number of weather stations varies significantly over time and none of the previously mentioned strategies are suitable, an Empirical Modelling Approach (EMA) can offer a potential solution. The EMA combines human expertise with statistical techniques to capture the historical information contained in available station time series, enabling the transfer of point-scale data to larger-scale MAP predictions. EMA can involve two main modes: one focuses on understanding how equations and parameters of dynamic models change with scale [28,29], while the other emphasises the best statistical representation and uncertainty representation [30], which is the main focus of this article.

In this study, we employed the EMA approach using a statistical Multivariate-Regression Process Model (hereafter MRPM) to analyse the entire spatial domain of the Calore River Basin (CRB), in Southern Italy. At the transition between the central and southern Italian Apennines, the CRB presents a notable division between two distinct areas with contrasting characteristics [31]. To the east, rainfall exhibits a relatively uniform distribution, while to the west, there is a notable rainfall gradient leading to higher precipitation values. Recognising the spatial heterogeneity inherent in the precipitation data, two observing stations were selected to represent the pluviometric conditions within the CRB: Benevento (BNOBS) for the flat areas and Montevergine (MVOBS) for the mountainous areas (Figure 1c). The orography of the CRB plays a crucial role in influencing the spatial pattern and amount of precipitation through various processes. As a result, precipitation increases with elevation, particularly on windward slopes, while the leeward side of mountain ranges experiences lower precipitation levels. By considering these factors, we aimed to capture the complex interplay between topography and precipitation in the CRB, allowing for a more comprehensive analysis of the region's hydrological dynamics.

This article is organised as follows. Section 2 introduces the data and methods used in this study: Section 2.1 provides an overview of the environmental setting, while Section 2.2 addresses the upscaling issue and outlines the solutions that have been applied to the CRB. Section 3 evaluates the model and presents the reconstructed annual MAP across the CRB

for the period 1869–2020. Finally, in Section 4, we conclude on research needs and the practical implications of spatio-temporal scaling.

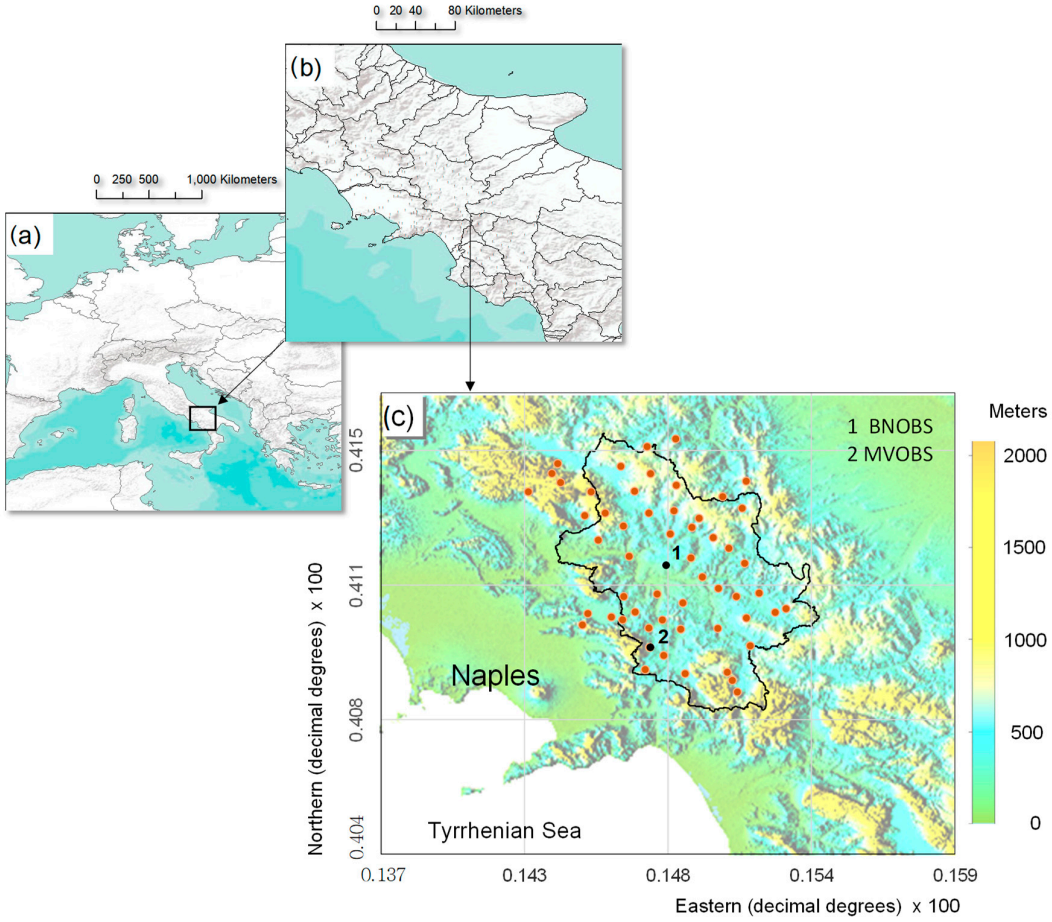

Figure 1. (**a**,**b**) Geographical setting of the study area (adapted from ArcGIS ESRI-Map via Geological Survey of Italy, Portal, http://sgi2.isprambiente.it/viewersgi2) (accessed on 28 June 2023); (**c**) Hill-shade layer of the Calore River Basin and surrounding lands showing the pluviometric network used for estimating Mean Areal Precipitation (the stations used for model calibration include Benevento—BNOBS 1 and Montevergine—MVOBS 2), adapted from Global Mapper (https://www.bluemarblegeo.com/global-mapper) (accessed on 28 June 2023).

2. Data and Methods

2.1. Pluviometric Network and Reference Stations

The study area focuses on the Calore River Basin (CRB), located in Northern Campania, Southern Italy, covering an approximate area of 3000 km^2 (Figure 1a,b). The CRB is situated between 41°11′ North and 14°27′ East, representing the transition zone between the central and southern Italian Apennines. The elevation within the basin ranges from about 50 to 1800 m a.s.l. Due to its topographic variability, a pluviometric network was established in the CRB. The initial stations were set up around 1920, and, over time, additional stations were added. By the 1940s, the pluviometric network had reached its maximum consistency with 56 sites (Figure 1c). This network remained relatively stable until the 1980s, albeit with occasional gaps in data, such as between 1947 and 1954 and during other shorter periods. Among these stations, only two have the longest and most continuous data series to date. These are the Benevento Meteorological Observatory of Benevento (hereafter BNOBS), which commenced operations on 1 March 1869, under the guidance of Nicola Orazio Albino, and the Montevergine Sanctuary Meteorological Observatory, established a few years later in 1884 (marked as numbers 1 and 2 in Figure 1c).

The CRB features predominantly mountainous terrain in the western part, with peaks reaching elevations of 1400 m a.s.l. (in the Taburno massif) and 1700 m a.s.l. (in the Picentini mountain range). In contrast, the eastern region consists of lower relief, with some elevations reaching around 1000 m a.s.l. The topography of the area exhibits a diverse range of elevations. Approximately 27% of the land is situated below 300 m a.s.l., while 36% consists of hills ranging between 300 and 600 m a.s.l. Another 23% is characterized by elevations between 600 and 900 m a.s.l., and the remaining 13% comprises mountainous areas exceeding 900 m a.s.l. These natural landscapes, already exhibiting a variety of forms, colours and textures, are further shaped by the presence of hills, mountains and villages that dot the landscape around the Calore River and its tributaries.

The instrumental precipitation data series of Benevento includes four distinct periods that follow the precipitation anomalies recorded since 1675 [32]. The first period covers 1 March 1869 to 31 December 1906, during which observations were conducted by Ambrogio Di Renzo. The second period encompasses the years from 1907 to 1947 and includes observations by Venanzio Vari, with the addition of Panfilo Boccabella. The third period encompasses the years from 1948 and 1968 and corresponds to the observations made by Nazario Doretti. The fourth period spans from 1969 to 2020 and consists of pluviometric surveys managed initially by the National Hydrographic and Mareographic Service until 1999, and later continued by the Meteorological Forecasting Functional Center of the Campania Region [32]. The Montevergine observatory (hereafter MVOBS) is the oldest among the high-altitude meteorological observatories located in Central and Southern Italy. It was established at the initiative of Barnabite Father Francesco Denza and has been managed by the Benedectine Community of Montevergine's Abbey. The first meteorological observations began under the guidance of Father Giuseppe Llobet, who served as the observer from 1884 to 1919. From 1920 to 1938, the directors of the observatory included Fathers Ildebrando Mancini, Ilario Mauro, Ugo Inzan and Giulio Corvino. In 1939, Father Virginio Cinella assumed responsibility for the observatory's services. The period of activity continued until 1961 [33]. Systematic observations resumed at the end of 1960 under the new direction of Father Amato Gubitosa and continued until 2006. Under the guidance of Father Andrea Komar and with the support of Dr. Vincenzo Capozzi, the Montevergine Observatory underwent significant renovations and modernisation after 2006. This included the installation of new equipment, including digital instruments, to enhance its capabilities. Since then, the updated data from the observatory have been based on the work of Capozzi and Budillon [34], as well as the Montevergine Observatory's official website (http://www.mvobsv.org) (accessed on 28 June 2023), which provides annual updates.

The variables used for model development include precipitation at BNOBS, the corresponding monthly standard deviation for each year, and precipitation at MVOBS. The years selected for model calibration (Figure 2, grey bands) were 1935–1942 and 1951–1977, during which the number of stations across the CRB varied slightly from year to year (mean: 37 ± 6 standard deviation). For model validation, the years chosen were 1978–1993, which exhibited greater variability in the number of stations (mean: 43 ± 11 standard deviation). The years between 1943 and 1950 were not included in the calibration stage due to many stations temporally ceasing their activity during the World War II. It should be noted that for the validation process, we have also intentionally excluded a group of years that may be less reliable and not fully representative of the CRB. This is due to the varying number of stations used annually to calculate the Actual Mean Areal Precipitation across the Calore River Basin, AMAP(CRB). Furthermore, after 1993, the pluviometric network in Campania experiences a significant and gradual decrease in the number of stations. For this reason, we did not extend the validation time series beyond this date.

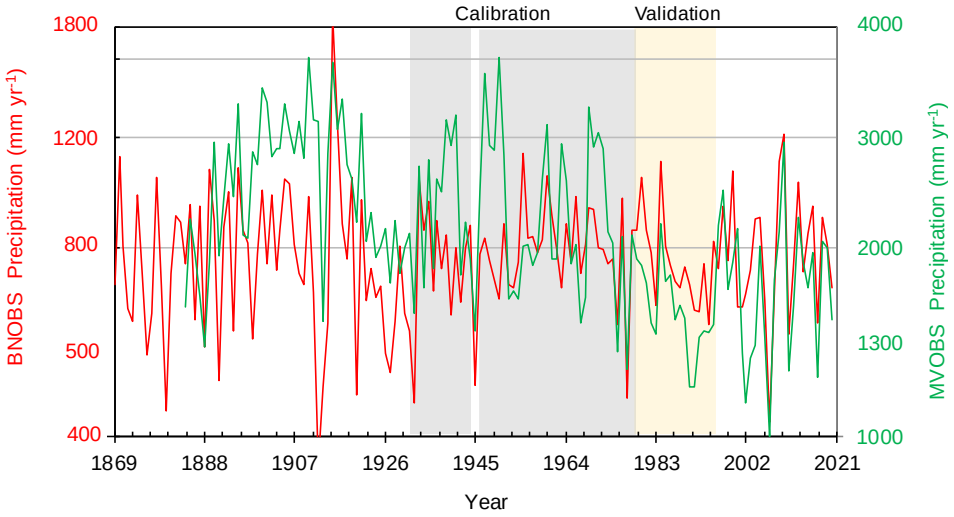

Figure 2. Temporal evolution of annual rainfall amount at station of Benevento (BNOBS, in red) and Montevergine (MVOBS, in green), with related periods (grey bands) used for model calibration and validation (yellow band). The *y*-axes are in log units. To determine the annual precipitation for 1869, we filled in the missing data of BNOBS for January and February using long-term monthly means.

2.2. Climate and Seasonal Regime Patterns

The activity of precipitation systems in the CRB is influenced by the convergence of moist air masses associated with different cyclonic situations, which occur when air masses with varying thermal characteristics meet in the central Mediterranean basin. The climate in this part of southern Italy is influenced by the complex interactions between cold air masses of northern Europe and tropical air masses, which give rise to Mediterranean cyclogenesis [35]. These depressions have the greatest impact on northern Italy and the Tyrrhenian coast, resulting in significant rainfall variability (Figure 3a).

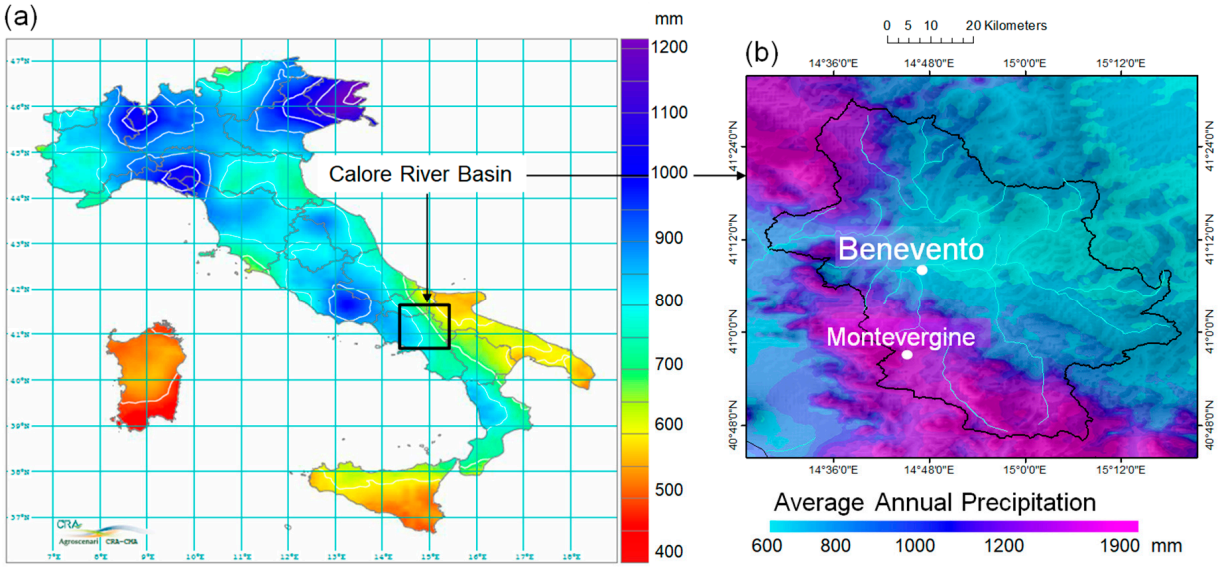

Figure 3. (**a**) Spatial pattern of mean annual precipitation over Italy during the period 1981–2010 (source: https://www.reterurale.it/flex/cm/pages/ServeBLOB.php/L/IT/IDPagina/16319) (accessed on 28 June 2023); (**b**) related downscaling across the Calore River Basin (black watershed). The downscaling was performed using an ordinary cokriging interpolator with a DEM (1 km resolution) as a covariate, employing ArcGIS ESRI software. The figure also includes the representation of the main river network (shown in blue) and the locations of Benevento (BNOBS) and Montevergine (MVOBS) stations used in this study.

By adjusting the spatial scale to focus on the area under study, we can appreciate a more detailed representation of precipitation variability across the CRB (Figure 3b). Consequently, the CRB exhibits a distinct divide between two contrasting areas. The eastern region experiences relative uniform precipitation patterns (Figure 3b, blue shape), with slightly higher amounts near the Apennine watershed (up to 900–1000 mm yr^{-1}). In contrast, the western region displays a significant pluviometric gradient, resulting in higher rainfall values (Figure 3b, violet band). These differences can be attributed to variations in altitude, geographic positioning, and the direction of the moist air flows. When precipitation systems encounter the sub-Apennine chain, they undergo enhanced water vapour condensation, leading to greater rainfall amounts before progressing eastwards into the basin's interior.

Considerable rainfall occurs throughout the summer in continental Campania, particularly from May to September, often in the form of showers and thunderstorms. It is worth mentioning that in Benevento, and on the central-eastern slopes in general, heavy rainfall (>20 mm d^{-1}) can occur due to both cold occlusions originating from the east and the passage of storms from the west. The south-western perturbed flows, which occur more frequently in the extreme western sectors of the CRB (such as Claudina valley, Partenio mountains, valley Teleseina and areas of Matese-Titerno), release their higher moisture content. As these flows progress towards the innermost areas of the CRB, they bring modest quantities of rainfall, generally ranging from 10 to 20 mm d^{-1} [36].

The CRB exhibits four distinct seasons from a bioclimatic perspective (Figure 4). The first is the humid and cold season, which spans from January to April. This is followed by the growth season, occurring from April to July. The dry season dominates from July to September. It is only after mid-September that the humid season begins, and from October to December, the Atlantic perturbations bring rains back with maximum abundance in a more consistent manner.

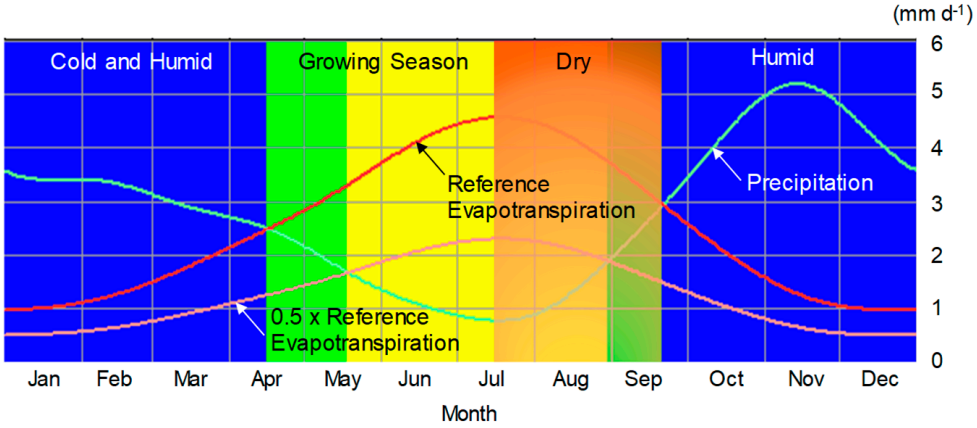

Figure 4. Seasonal climogram depicting various monthly elements of the water balance for the Calore River Basin during the period 1961–1990. The climogram was created using the FAO–LocClim 1.0 software. The blue bands indicate cold and humid seasons. The green and yellow bands distinguish between the first part (spring) and the second part of the growing season. Orange to orange-greed degraded bands indicate the progression of the dry season.

2.3. Mean Areal Annual Precipitation (AMAP) Data

To determine the actual mean areal precipitation for the years when a sufficient number of stations (up to 56) were available across the CRB, we derived the corresponding AMAP values using the Thiessen approach, which is a direct weighted average method that involves dividing a region into sub-regions centred on each monitoring site [37]. Although the sub-basins do not align perfectly with the Thiessen sub-regions, it is possible to calculate the fraction of each Thiessen sub-region that contributes to each sub-basin. This allows

for the computation of weighted averages to estimate the AMAP for each sub-basin. The equations used to compute the spatial average are as follows [38]:

$$\text{AMAP} = \frac{1}{\text{A}} \times \sum_{g=1}^{G} a_g \times P_g \quad (1)$$

$$\sum_{g=1}^{G} a_g = 1 \quad (2)$$

where AMAP is the actual mean areal precipitation for G gauges, denoted as $g = 1, \ldots, G$; P_g (mm yr^{-1}) is the precipitation measured at each gauge; a_g (km^2) is the area of each sub-region, whose sum is the total area of the basin (A = 3058 km^2).

2.4. Model Development

The varied topography of the basin can modify local precipitation patterns. The influence of precipitation change on a larger scale is determined by the spatial and temporal scale of disturbances, as well as the interplay between disturbances and the small-scale landscape variability [20].

Orographic precipitation, which is prominent in mountainous river basins, exhibits a substantial spatial variability. Consequently, mean areal precipitation is scale-dependent and statistically non-homogeneous in space [39]. To minimise uncertainty in estimating the annual MAP across the CRB, MAP(CRB), we have employed a multivariate linear regression approach with three variables and four parameters. This enables us to examine the relationship between a response variable (AMAP) and one or more predictor variables, e.g., P(BNOBS) and P(MVOBS). By understanding how changes in predictor variables are associated with changes in the response variable, we can estimate the value of the response variable based on the known values of the predictor variables [40].

From this sample, our initial focus was on gaining a comprehensive understanding of the factors that potentially influence the amount and spatial-temporal distribution of precipitation in each year. We engaged an iterative process, employing a trial-and-error approach to identify the relevant drivers and develop an explanation for the long-term dynamics of areal precipitation in a relatively simplified manner. This involved a stepwise approach, systematically adding and removing terms as needed. As we progressed, we incorporated more complex terms while adhering to the principle of parsimony, ensuring that the model included only a limited number of factors for a MRPM. The following approach was thus formulated for estimating MAP(CRB):

$$\text{MRPM}_{\text{MAP(CRB)}} = \alpha \times (P(\text{BNOBS}) - \vartheta \times \text{SDP}(\text{BNOBS})) + \beta \times \left(\frac{\text{P(MVOBS)}}{\text{P(BNOBS)} - \text{C}}\right) + \gamma \quad (3)$$

The parameters of Equation (3), α, β, ϑ (scale factors), γ (position factor) and C (linearisation factor), were optimised through a co-iterative calibration process against AMAP(CRB) values derived from the Thiessen method. The monthly standard precipitation (SDP) calculated for Benevento station, SDP(BNOBS), served as a determinant factor. A higher SDP(BNOBS) indicates not only deficient rainfall at BNOBS but also a higher likelihood of drought across the CRB. The precipitation ratio, represented in the third term, provides insights into the precipitation pattern across the CRB. A ratio close to 1 suggests attenuated precipitation over the CRB, while a ratio significantly greater than 1 indicates increased precipitation. This ratio captures the extent of the precipitation system over the basin, with a higher ratio indicating a larger coverage area. The factors contributing to this ratio can be explained as follows: (1) the sub-Apennine chain is situated to the west of the CRB, which is typically the direction from which precipitation systems originate. If there is a substantial difference in rainfall between Montevergine and Benevento, it indicates the recurrence of disturbances during that particular year; (2) Montevergine represents meteorological conditions at higher altitudes, while Benevento represents conditions in

a flat area. Thus, the ratio aims to consider the overall frequency, duration and quantity of precipitation systems affecting the CRB, taking into account both altitude-related meteorological conditions and disturbances originating from the sub-Apennine chain.

The calibration process focused on maximising the goodness-of-fit (R^2) of the linear regression between the actual and estimated MAP data (and the linear correlation coefficient $r = \sqrt{(R^2)}$. The optimum value for R^2 is 1. Additionally, the Nash-Sutcliffe (NSI) efficiency index [41] was maximised. The NSI, with an optimum value of 1, extends the R^2 statistics to assess the relative accuracy of predictions from any class of models, where values below zero indicate worse performance than a simple mean estimation and values above zero indicate better performance. The mean absolute error (MAE) was also calculated to quantify the amount of error. Skewness and kurtosis metrics were examined to evaluate the distribution of the data and assess the departure from normality. In addition, a range of statistical tests were conducted to provide a comprehensive analysis of the model's performance. The two-sided Kolmogorov–Smirnov test [42] was used to compare the distribution of observed and predicted values. The Durbin–Watson test [43] was employed to examine residual autocorrelation. Student's *t*-test [44] and Wilcoxon (1945) test [45] were utilised for comparing means between different groups. Lastly, the Kendall [46] test was employed for trend analysis together with Buishand [47] test to assess the presence of any systematic changes over time.

The data processing, interpretation, and exploration of patterns and relationships were conducted by leveraging the capabilities of spreadsheet-based tools and statistical software. Various statistical test and analysis were conducted, using the online software STATGRAPHICS (http://www.statpoint.net/default.aspx) (accessed on 28 June 2023) and VassarStats (http://vassarstats.net) (accessed on 28 June 2023). Additionally, graphical support for data visualisation and analysis was obtained from AnClim (http://www.climahom.eu/software-solution/anclim; [48]) (accessed on 28 June 2023) and CurveExpert Professional 1.6 (https://www.curveexpert.net) (accessed on 28 June 2023).

3. Results and Discussion

In this section, we evaluate the performance of the MRPM in capturing geographically referenced precipitation variables across the basin area. We begin by examining the calibration stage in Section 3.1, assessing how well the model reproduces observed precipitation patterns. We then extend our evaluation to the validation stage, ensuring the reliability of the model in replicating precipitation patterns. Finally, a comparative analysis between the MRPM and an alternative (simplified) modelling approach is performed to determine their respective performances and the potential for simplifying Equation (3). Lastly, in Section 3.2, we present a historical simulation obtained using the calibrated model to gain additional insights into its capabilities.

3.1. Model Parameterisation and Evaluation

The multivariate regression equation, Equation (3), achieved the best fit for the estimated AMAP(CRB) data with the parameter values $\alpha = 1.196$, $\beta = 116.3$, $\vartheta = 2$, $\gamma = 256$, and $C = 275$. During calibration (31 years), one outlier data value, represented by the red point in the scatterplot of Figure 5a, was excluded. The analysis of the calibration set indicates a significant relationship (F-test $p < 0.05$) between the actual and estimated data, demonstrating the satisfactory performance of the MRPM model with an NSI of 0.85 and an R^2 of 0.72 ($r = 0.85$). The mean absolute error (MAE), used to quantify the amount of error, was found to be 68 mm, lower than the standard deviation of the residuals (90 mm). The Durbin–Watson (DW) statistic ($DW = 1.61$; $p = 0.12$) indicated that there is no evidence of serial autocorrelation in the residuals. Figure 5b shows an approximated normal distribution of model residuals while Figure 5c depicts a quantile–quantile plot with points closely aligning with the expected line, indicating a potential normal distribution of population values, except for a few extreme positive values that appear to depart from this pattern.

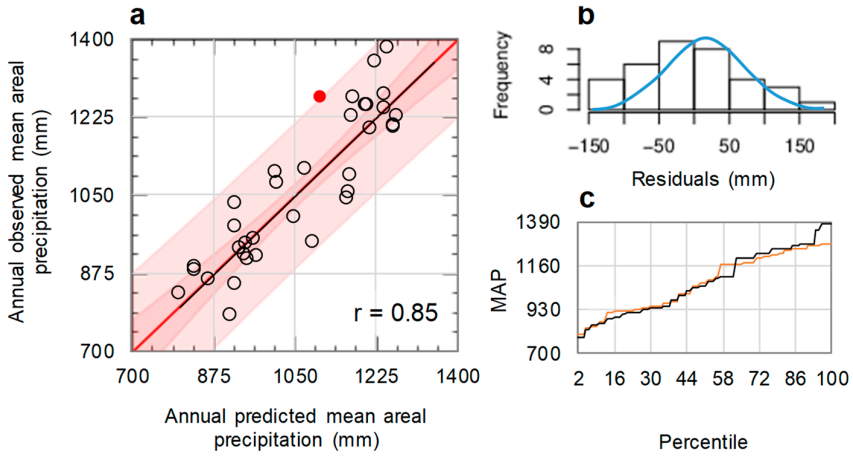

Figure 5. (**a**) Scatterplot of observed and predicted mean areal precipitation at the calibration stage using the MRPM model, Equation (3), for the periods 1937–1942 and 1951–1976 in the Calore River Basin; the inner bounds represent 90% confidence limits (pink coloured area), while the outer bounds represent 95% prediction limits for new observations (the red data-point indicates the outlier; (**b**) histogram of residuals showing a Gaussian shape (blue line); (**c**) observed percentile (black line) and predicted percentile distribution (orange line).

Both the standardised values of skewness and kurtosis, falling within the expected range of −2 to +2, indicate no significant departures from normality (Table 1). Additionally, the Kolmogorov–Smirnov (KS) test yielded an estimated overall statistic (DN) of 0.11, a two-sided large sample KS statistic of 0.48, and an approximate *p*-value of 0.98, providing no statistically significant difference between the two distributions.

Table 1. Standardised skewness and kurtosis values.

Statistics	MAP_{Mod}	MAP_{Obs}	MAP_{Mod}	MAP_{Obs}
Stnd. skewness	−0.29	0.28	1.68	1.97
Stnd. kurtosis	−1.73	−1.52	0.09	0.67

The validation set analysis (Figure 6a) reveals a significant relationship (F-test $p < 0.05$) between the actual and estimated data, with an R^2 value of 0.70 indicating a strong correlation (r = 0.84). Furthermore, the NSI value of 0.70 and the MAE value of 107 mm (lower than the standard deviation of the residuals, which is 134 mm) provide additional support for the reliability of the MRPM. The Durbin–Watson (DW) test (1.75, $p = 0.31$) suggests no serial autocorrelation in the residuals. Furthermore, the quantile–quantile plot in Figure 6c indicates an approximately normal population distribution, despite a slight deviation observed in the histogram of Figure 6b. The standardised values of skewness and kurtosis, falling within the expected range of −2 to +2, also support the absence of significant deviations from normality (Table 1). Furthermore, the Kolmogorov–Smirnov (KS) test yielded an estimated overall statistic (DN) of 0.13 and a two-sided large sample KS statistic of 0.35 ($p > 0.99$), indicating that there is no statistically significant difference between the two compared distributions. Overall, the somewhat lower accuracy observed in the validation stage (14 years), in comparison to the calibration set, can be attributed to the reduced number of stations in the pluviometric network.

Finally, to assess the possibility of simplifying the MRPM model, we conducted a multiple linear regression analysis using the equation $W = A \cdot X1 + B \cdot X2 + C \cdot X3 + D$. This equation aims to capture the relationship between mean areal precipitation W and the three independent components in Equation (3): $X1$ representing precipitation associated with standard deviation, $X2$ representing precipitation at BNOBS and $X3$ representing the variable associated with ratios between MVOBS and BNOBS precipitation. After recalibrating the MRPM, we found that even the term $X1$, with the highest *p*-value of 0.001, remains

statistically significant. Consequently, the model represented by Equation (3) cannot be simplified, indicating that it remains stable, interpretable and applicable, consistent with the criteria set by Royston and Sauerbrei [49].

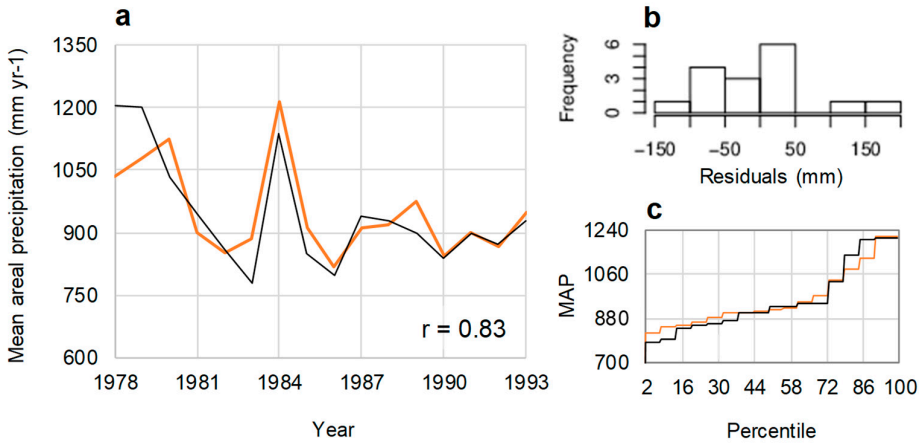

Figure 6. Model performance at the validation stage of the mean areal precipitation, Equation (3), for the Calore River Basin. (**a**) Evolution of actual (black line) and predicted (orange line) precipitation; (**b**) histogram of residuals; (**c**) observed percentile (black line) and predicted percentile distribution (orange line).

3.2. Reconstructed Rainfall Variability

To establish the climatic context from which the basin has evolved, it is important to provide an overview of the historical development of precipitation in the CRB before discussing the instrumental MAP(CRB) time-series. During the analysis of the pre-instrumental period, Diodato [32] utilised normalised cumulative anomalies to examine the prevalence of negative and positive annual anomalies, enabling the identification of major turning points and the study of extreme weather events in relation to atmospheric circulation patterns over time. It is noteworthy that the effects of the Little Ice Age (approximately the 14th to 19th century) were not uniform in Southern Italy. The period from 1798 to 1919 exhibited a generally wet climate, while the periods of 1710–1797 and 1920–2002 were characterised by relatively dry conditions and reduced variability. The transition from 1798 to 1919 may have been influenced by the introduction of particulate matter into the atmosphere, possibly originating from volcanic activity. This underscores the intricate interplay of regional variability, the Little Ice Age and external factors in shaping precipitation trends during the pre-instrumental period in Southern Italy. Next, we present the instrumental MAP(CRB) time-series. Figure 7a depicts its statistical characteristics. The long-term mean of the series is found to be 1086 $\pm$ 179 mm. However, this value is relative due to a break-point around the year 1951. This break-point divides the series in two sub-series with slightly different mean values, as indicated by the dashed lines in Figure 7a.

A climatic shift, as identified by the Buishand test (grey line in Figure 7a), reveals mean values of 1153 $\pm$ 168 mm for the first period from 1869 to 1951 and 998 $\pm$ 147 mm for the second and more recent period from 1952 to 2020. This shift is accompanied by a decrease in the mean value between the two periods and a reduction in interannual variability around the mean. The difference in mean values was found to be statistically significant ($p < 0.0001$) according to the non-parametric Mann–Whitney test, considering unequal sample sizes. To further investigate this trend, a correlation plot test based on Kendall tau rank correlations was performed. The test yielded a negative and significant Kendall tau value of -0.263, indicating a decrease of 215 mm over the 148-year period. The analysis of rainfall statistics reveals that the highest rainfall values occurred in 1915, with both BNOBS and MVOBS recording the maximum values in the entire time-series, reaching 2084 mm. This peak was recorded during a wet period preceding 1915. Conversely, the minimum value of 737 mm

was recorded in 2011, following a notably dry period around the year 1990. Based on these findings, we conclude that the MAP series in the CRB underwent a significant change, with a pivotal point identified around the year 1951. This specific year marks the division of the series with distinct frequency distributions, as depicted in Figure 7b,c.

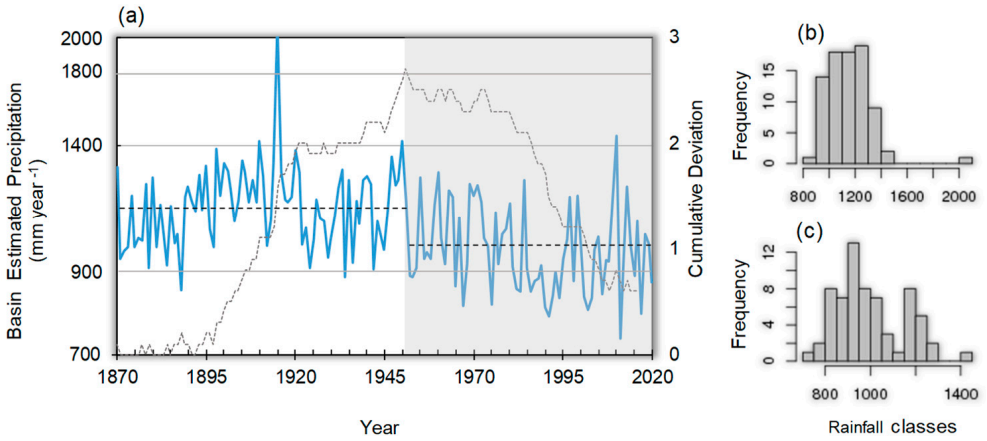

Figure 7. (**a**) Temporal evolution of the estimated mean areal precipitation over the Calore River Basin from 1869 to 2020 (blue line), with the relative cumulative deviation (grey line) highlighting a climatic shift around the year 1951. The dashed lines represent the mean values before and after this break-point (respectively, indicated on the left y-axis in log units); (**b**) absolute frequency distribution for the period 1869–1951; (**c**) absolute frequency distribution for the period 1952–2020.

For the first period from 1869 to 1951, the frequency distribution of MAP in the CRB exhibits a pseudo-Gaussian and unimodal pattern, with a higher absolute frequency observed around the rainfall class of 1200 mm (Figure 7b). In contrast, the second period from 1952 to 2020 shows a discernible bimodal distribution. This bimodality suggests that the recent period experiences a more diverse range of precipitation patterns operating over the basin compared to the earlier period. It can be hypothesised that in the past, the CRB was influenced by more homogeneous precipitation systems, while the current warming phase may contribute to localised and inhomogeneous climatic conditions. This could potentially exacerbate environmental challenges in vulnerable areas and lead to difficulties in accurately measuring intense and localised rainfall due to limited coverage of the pluviometric networks [50].

4. Conclusions and Perspectives

In this study, we successfully applied the Multivariate-Regression Process Model (MRPM) to capture and replicate precipitation patterns in the Mediterranean basin of the Calore River. Our analysis revealed a significant climatic shift around 1951, indicating that the recent period exhibits a greater diversity of precipitation patterns compared to the earlier period. This finding emphasizes the need to consider the complexity of precipitation processes and their impacts on the local environment. Understanding these dynamics is crucial for effective water resource management, agriculture, and ecosystem conservation in the Calore River Basin.

The observed climate shifts and changes in precipitation patterns have important implications for adaptation in the face of evolving climate conditions. Future research should focus on refining the MRPM by optimising model parameters and incorporating additional variables or data sources. This would enhance the model's performance and provide a more comprehensive understanding of precipitation patterns across various regions. Furthermore, investigating the drivers behind the identified climatic shift and its implications for local ecosystems and communities is essential. This knowledge would facilitate climate adaptation and resilience planning, ensuring the sustainability of natural resources and human well-being.

To improve the accuracy and reliability of precipitation modelling, efforts should be made to expand the pluviometric network and enhance data collection and monitoring systems. The observed lower accuracy in the validation stage, attributed to the reduced number of stations in the dataset, underscores the importance of maintaining and expanding observational networks. Increasing the spatial and temporal coverage of precipitation data will enable more accurate assessments and modelling at different scales.

Overall, this study contributes valuable insights into geographically referenced precipitation variables and their implications in the Calore River Basin. The findings inform decision-making processes and support the development of sustainable water resource management strategies in response to changing precipitation patterns and climate conditions. By continually advancing our understanding of precipitation dynamics, we can foster resilience and ensure the long-term viability of ecosystems and communities in the face of a changing climate.

Author Contributions: Conceptualisation, N.D.; methodology, N.D. and G.B.; formal analysis, N.D.; data curation, N.D.; writing—original draft preparation, N.D.; writing—review and editing, N.D. and G.B.; supervision, G.B. All authors have read and agreed to the published version of the manuscript.

Funding: This research received no external funding.

Data Availability Statement: Research data can be provided on request to authors.

Conflicts of Interest: The authors declare no conflict of interest.

References

1. Abatzoglou, J.T.; Dobrowski, S.Z.; Parks, S.A.; Hegewisch, K.C. TerraClimate, a high-resolution global dataset of monthly climate and climatic water balance from 1958–2015. *Sci. Data* **2018**, *5*, 170191. [CrossRef]
2. Korell, L.; Auge, H.; Chase, J.M.; Harpole, W.S.; Knight, T.M. Responses of plant diversity to precipitation change are strongest at local spatial scales and in drylands. *Nat. Commun.* **2021**, *12*, 2489. [CrossRef] [PubMed]
3. Wang, D.; Alimohammadi, N. Responses of annual runoff, evaporation, and storage change to climate variability at the watershed scale. *Water Resour. Res.* **2012**, *48*, W05546. [CrossRef]
4. Pavlovic, S.; Perica, S.; St Laurent, M.; Mejia, A.; Knight, T.M. Intercomparison of selected fixed-area areal reduction factor methods. *J. Hydrol.* **2016**, *537*, 419–430. [CrossRef]
5. Kim, J.; Lee, J.; Kim, D.; Kang, B. The role of rainfall spatial variability in estimating areal reduction factors. *J. Hydrol.* **2019**, *568*, 416–426. [CrossRef]
6. Guo, B.; Zhang, J.; Meng, X.; Xu, T.; Song, Y. Long-term spatio-temporal precipitation variations in China with precipitation surface interpolated by ANUSPLIN. *Sci. Rep.* **2020**, *10*, 81. [CrossRef]
7. Wu, Z.; Dijkstra, P.; Koch, G.W.; Hungate, B.A. Biogeochemical and ecological feedbacks in grassland responses to warming. *Nat. Clim. Chang.* **2012**, *2*, 458–461. [CrossRef]
8. Diffenbaugh, N.S.; Field, C.B. Changes in ecologically critical terrestrial climate conditions. *Science* **2013**, *341*, 486–492. [CrossRef]
9. Jung, M.; Reichstein, M.; Ciais, P.; Seneviratne, S.I.; Sheffield, J.; Goulden, M.L.; Bonan, G.; Cescatti, A.; Chen, J.; de Jeu, R.; et al. Recent decline in the global land evapotranspiration trend due to limited moisture supply. *Nature* **2010**, *467*, 951–954. [CrossRef]
10. Good, S.P.; Noone, D.; Bowen, G. Hydrologic connectivity constrains partitioning of global terrestrial water fluxes. *Science* **2015**, *349*, 175–177. [CrossRef]
11. Duffy, C.J. The terrestrial hydrologic cycle: An historical sense of balance. *Wires Water* **2017**, *4*, e1216. [CrossRef]
12. Zeng, Q.; Chen, H.; Xu, C.-Y.; Jie, M.-X.; Chen, J.; Guo, S.-L.; Liu, J. The effect of rain gauge density and distribution on runoff simulation using a lumped hydrological modelling approach. *J. Hydrol.* **2018**, *563*, 106–122. [CrossRef]
13. Kursinski, A.L.; Zeng, X. Areal estimation of intensity and frequency of summertime precipitation over a midlatitude region. *Geophys. Res. Lett.* **2006**, *33*, L22401. [CrossRef]
14. Price, K.; Purucker, S.T.; Kraemer, S.R.; Babendreier, J.E.; Knightes, C.D. Comparison of radar and gauge precipitation data in watershed models across varying spatial and temporal scales. *Hydrol. Process.* **2014**, *28*, 3505–3520. [CrossRef]
15. Donnelly, C.; Ernst, K.; Arheimer, B. A comparison of hydrological climate services at different scales by users and scientists. *Clim. Serv.* **2018**, *11*, 24–35. [CrossRef]
16. Abatzoglou, J.T. Development of gridded surface meteorological data for ecological applications and modelling. *Int. J. Climatol.* **2011**, *33*, 121–131. [CrossRef]
17. Easterling, D.R.; Kunkel, K.E.; Wehner, M.F.; Sun, L. Detection and attribution of climate extremes in the observed record. *Weather Clim. Extrem.* **2016**, *11*, 17–27. [CrossRef]
18. Wainwright, J.; Mulligan, M. *Environmental Modelling: Finding Simplicity in Complexity*, 2nd ed.; John Wiley & Sons, Ltd.: Hoboken, NJ, USA, 2013.

19. Okkan, U. Assessing the effects of climate change on monthly precipitation: Proposing of a downscaling strategy through a case study in Turkey. *KSCE J. Civ. Eng.* **2015**, *19*, 1150–1156. [CrossRef]
20. Harvey, L.D.D. Upscaling in global change research. *Clim. Chang.* **2000**, *44*, 225–263. [CrossRef]
21. Piras, M.; Mascaro, G.; Deidda, R.; Vivoni, E.R. Impacts of climate change on precipitation and discharge extremes through the use of statistical downscaling approaches in a Mediterranean basin. *Sci. Total Environ.* **2016**, *543*, 952–964. [CrossRef] [PubMed]
22. Ashouri, H.; Hsu, K.-L.; Sorooshian, S.; Braithwaite, D.K.; Knapp, K.R.; Cecil, K.D.; Nelson, B.R.; Prat, O.P. PERSIANN-CDR: Daily precipitation climate data record from multisatellite observations for hydrological and climate studies. *Bull. Am. Meteorol. Soc.* **2015**, *96*, 69–83. [CrossRef]
23. Tang, Q.; Gao, H.; Lu, H.; Lettenmaier, D.P. Remote sensing: Hydrology. *Prog. Phys. Geogr.* **2009**, *33*, 490–509. [CrossRef]
24. Sood, A.; Smakhtin, V. Global hydrological models: A review. *Hydrol. Sci. J.* **2015**, *60*, 6667. [CrossRef]
25. Karger, D.K.; Conrad, O.; Böhner, J.; Kawohl, T.; Kreft, H.; Soria-Auza, R.W.; Zimmermann, N.E.; Linder, H.P.; Kessler, M. Climatologies at high resolution for the earth's land surface areas. *Sci. Data* **2017**, *4*, 170122. [CrossRef]
26. Breinl, K.; Di Baldassarre, G.; Lopez, M.G.; Hagenlocher, M.; Vico, G.; Rutgersson, A. Can weather generation capture precipitation patterns across different climates, spatial scales and under data scarcity? *Sci. Rep.* **2017**, *7*, 5449. [CrossRef]
27. Ali, G.; Sajjad, M.; Kanwal, S.; Xiao, T.; Khalid, S.; Shoaib, F.; Gul, H.N. Spatial–temporal characterization of rainfall in Pakistan during the past half-century (1961–2020). *Sci. Rep.* **2021**, *11*, 6935. [CrossRef] [PubMed]
28. Merz, R.; Parajka, J.; Blöschl, G. Scale effects in conceptual hydrological modelling. *Water Resour. Res.* **2009**, *45*, W09405. [CrossRef]
29. Del Giudice, D.; Albert, C.; Rieckermann, J.; Reichert, P. Describing the catchment-averaged precipitation as a stochastic process improves parameter and input estimation. *Water Resour. Res.* **2016**, *52*, 3162–3186. [CrossRef]
30. Zhang, A.; Shi, H.; Li, T.; Fu, X. Analysis of the influence of rainfall spatial uncertainty on hydrological simulations using the bootstrap method. *Atmosphere* **2018**, *9*, 71. [CrossRef]
31. Diodato, N. Ricostruzione storica dei rilevamenti pluviometrici nell'Italia peninsulare: Il caso dell'Osservatorio Meteorologico di Benevento—Centro Storico (1869–1999). *Boll. Geofis.* **2002**, *25*, 27–44. (In Italian)
32. Diodato, N. Climatic fluctuations in Southern Italy since the 17th century: Reconstruction with precipitation records at Benevento. *Clim. Chang.* **2007**, *80*, 411–431. [CrossRef]
33. Diodato, N. Montevergine: Unica vedetta storica dell'Appennino fondata per mezzo di Padre Francesco Denza. *Boll. Geofis.* **1995**, *18*, 47–51. (In Italian)
34. Capozzi, V.; Budillon, G. Time series analysis of climatological records from a high altitude observatory in Southern Italy (Montevergine, AV). In Proceedings of the First Annual Conference "Climate Change and Its Implications on Ecosystem Services and Society", Lecce, Italy, 22–23 September 2013; Società Italiana per le Scienze del Clima: Lecce, Italy, 2013; pp. 1–25.
35. Buzzi, A.; Tosi, E. Statistica dei transienti atmosferici in area Mediterranea. *Boll. Geofis.* **1991**, *14*, 87–93. (In Italian)
36. Diodato, N.; Ceccarelli, M.; Bellocchi, G. Decadal and century-long changes in the reconstruction of erosive rainfall anomalies at a Mediterranean fluvial basin. *Earth Surf. Process. Landf.* **2008**, *33*, 2078–2093. [CrossRef]
37. Thiessen, A.H. Precipitation averages for large areas. *Mon. Weather Rev.* **1911**, *39*, 1082–1089. [CrossRef]
38. Zeiger, S.; Hubbart, J. An assessment of mean areal precipitation methods on simulated stream flow: A SWAT model performance assessment. *Water* **2017**, *9*, 459. [CrossRef]
39. Salas, J.D.; Govindaraju, R.S.; Anderson, M.; Arabi, M.; Francés, F.; Suarez, W.; Lavado-Casimiro, W.S.; Green, T.R. *Handbook of Environmental Engineering, Volume 15: Modern Water Resources Engineering*; Wang, L.K., Yang, C.T., Eds.; Springer Science & Business Media: New York, NY, USA, 2014; pp. 1–126.
40. Pardoe, I. *Applied Regression Modelling*; John Wiley & Sons, Inc.: Hoboken, NJ, USA, 2012.
41. Nash, J.E.; Sutcliffe, J.V. River flow forecasting through conceptual models part I—A discussion of principles. *J. Hydrol.* **1970**, *10*, 282–290. [CrossRef]
42. Smirnov, N. Table for estimating the goodness of fit of empirical distributions. *Ann. Mat. Stat.* **1948**, *19*, 279–281. [CrossRef]
43. Durbin, J.; Watson, G.S. Testing for serial correlation in least squares regression. III. *Biometrika* **1971**, *58*, 1–19. [CrossRef]
44. Student, B. The probable error of a mean. *Biometrika* **1908**, *6*, 1–25. [CrossRef]
45. Wilcoxon, F. Individual comparisons by ranking methods. *Biom. Bull.* **1945**, *1*, 80–83. [CrossRef]
46. Kendall, M. A new measure of rank correlation. *Biometrika* **1938**, *30*, 81–89. [CrossRef]
47. Buishand, T.A. Some methods for testing homogeneity of rainfall records. *J. Hydrol.* **1982**, *58*, 11–27. [CrossRef]
48. Štěpánek, P. *AnClim—Software for Time Series Analysis*; Faculty of Natural Sciences, Masaryk University: Brno, Czechia, 2005.
49. Royston, P.; Sauerbrei, W. *Multivariate Model-Building*; John Wiley & Sons, Ltd.: Chichester, UK, 2008.
50. Mazzarela, A.; Tranfaglia, G.; Di Donna, G. Il contributo della geometria frattale alla stima del deficit risolutivo di una rete di pluviometri e del rischio di piogge intense. *Boll. Geofis.* **1999**, *22*, 61–71. (In Italian)

Disclaimer/Publisher's Note: The statements, opinions and data contained in all publications are solely those of the individual author(s) and contributor(s) and not of MDPI and/or the editor(s). MDPI and/or the editor(s) disclaim responsibility for any injury to people or property resulting from any ideas, methods, instructions or products referred to in the content.